

MIT Open Access Articles

*X-Ray Spectroscopy of II Pegasi: Coronal
Temperature Structure, Abundances, and Variability*

The MIT Faculty has made this article openly available. **Please share**
how this access benefits you. Your story matters.

Citation: Huenemoerder, David P., Claude R. Canizares, and Norbert S. Schulz. "X-Ray Spectroscopy of II Pegasi: Coronal Temperature Structure, Abundances, and Variability." *The Astrophysical Journal* 559.2 (2001): 1135–1146.

As Published: <http://dx.doi.org/10.1086/322419>

Publisher: IOP Publishing

Persistent URL: <http://hdl.handle.net/1721.1/76180>

Version: Author's final manuscript: final author's manuscript post peer review, without publisher's formatting or copy editing

Terms of Use: Article is made available in accordance with the publisher's policy and may be subject to US copyright law. Please refer to the publisher's site for terms of use.



X-Ray Spectroscopy of II Pegasi: Coronal Temperature Structure, Abundances, and Variability

David P. Huenemoerder¹, Claude R. Canizares², and Norbert S. Schulz³
MIT Center for Space Research
70 Vassar St.,
Cambridge, MA 02139

ABSTRACT

We have obtained high resolution X-ray spectra of the coronally active binary, II Pegasi (HD 224085), covering the wavelength range of 1.5-25Å. For the first half of our 44 ksec observation, the source was in a quiescent state with constant X-ray flux, after which it flared, reaching twice the quiescent flux in 12 ksec, then decreasing. We analyze the emission-line spectrum and continuum during quiescent and flaring states. The differential emission measure derived from lines fluxes shows a hot corona with a continuous distribution in temperature. During the non-flare state, the distribution peaks near $\log T = 7.2$, and when flaring, near 7.6. High-temperature lines are enhanced slightly during the flare, but most of the change occurs in the continuum. Coronal abundance anomalies are apparent, with iron very deficient relative to oxygen and significantly weaker than expected from photospheric measurements, while neon is enhanced relative to oxygen. We find no evidence of appreciable resonant scattering optical depth in line ratios of iron and oxygen. The flare light curve is consistent with Solar two-ribbon flare models, but with a very long reconnection time-constant of about 65 ks. We infer loop lengths of about 0.05 stellar radii, to about 0.25 in the flare, if the flare emission originated from a single, low-density loop.

Subject headings: stars: coronae — stars: individual (II Pegasi) — X-rays: stars — stars: abundances — stars: activity — line: identification

1. Introduction

II Pegasi (HD 224085) is a 7.6 V magnitude spectroscopic binary comprised of a K2-3 V-IV star plus an unseen companion in a 6.7 day orbit (Strassmeier, et al. 1993; Berdyugina et al. 1998). II Peg is bright and active in the radio, optical, UV, and X-ray regions (Owen & Gibson 1978; Walter & Bowyer 1981; Schwartz et al. 1981). It was discovered as photometrically variable by Chugainov (1976), and was classified as an RS CVn system by Rucinski (1977) based on the photometric properties and by nature of its strong optical emission lines.

It has been known for quite some time that

the RS CVn class is very luminous in X-rays and that this luminosity is strongly correlated with stellar rotation (Walter & Bowyer 1981). The working paradigm is that the photometric and spectroscopic features are due to scaled-up versions of Solar type “activity”: dark photospheric spots, bright chromospheric plages and prominences, a UV-bright transition region, an X-ray-bright corona, and variability from short-lived flares to long-term cycles.

One of the fundamental outstanding problems of stellar activity is the nature of the underlying coronal heating mechanisms, which are ultimately tied to the stellar rotation and a magnetic dynamo. We cannot observe these directly but infer their presence through observations of the energy emitted, correlations with fundamental stellar parameters, and through time variability. The *Chan-*

¹dph@space.mit.edu

²crc@space.mit.edu

³nss@space.mit.edu

Chandra High Energy Grating Spectrometer (HETGS) provides new capabilities in X-ray spectroscopy, giving us much enhanced spectral resolving power and sensitivity than previous X-ray observatories. Its performance is complementary to other current instruments such as the *Chandra* Low Energy Grating Spectrometer and the *XMM* Reflection Grating Spectrometer.

The *Chandra* HETGS spectra of II Peg provide new and definitive information in several key areas pertinent to the hottest part of the outer stellar atmosphere, the corona: the coronal iron abundance is low; the differential emission measure is continuous in temperature; flare time profiles are consistent with Solar two-ribbon flare models and are very hot. Here we present the HETGS spectrum, line flux measurements, differential emission measure and abundance fits, density diagnostics, a model spectrum, and line and continuum light-curves.

2. Observations and Data Processing

2.1. The *Chandra* HETGS

The HETG assembly (Markert et al. 1994; Canizares, et al. 2001) is comprised of an array of grating facets that can be placed into the converging X-ray beam just behind the *Chandra* High Resolution Mirror Assembly (HRMA). When in place, the gratings disperse the X-rays creating spectra that are recorded at the focal plane by the spectroscopic array, “S”, of ACIS (Advanced CCD Imaging Spectrometer). There are two different grating types, designated MEG and HEG, optimized for medium and high energies, respectively, which overlap in spectral coverage. The HETGS provides spectral resolving power of $\lambda/\Delta\lambda = 100 - 1000$. The line width is about 0.02 Å for MEG, and 0.01 Å for HEG (full widths, half maximum). The effective area is 1-180 cm² over the wavelength range of 1.2-25 Å (0.4-10 keV). Multiple overlapping orders are separated using the moderate energy resolution of the ACIS detector. (For detailed descriptions of the instrument we refer you to the “Proposers’ Observatory Guide,”⁴).

⁴Available from <http://cxc.harvard.edu/udocs/docs/docs.html>

2.2. The Observation

II Peg was observed on 17-18 October, 1999 (observation identifier 1451, Sequence Number 270401). At the time of the observation, the ACIS camera had a problem with one of its Front End Processors (FEP). This required the omission of one of the six CCDs of ACIS-S from telemetry. The S0 chip, at the longest wavelength on the negative order side was switched off, with a corresponding loss of some spectral coverage not redundant with the plus side and some effective area where plus and minus overlap. The observation was otherwise done in nominal, timed-exposure mode.

The count rate in the dispersed order region is about 3 counts s⁻¹, averaged over the length of good exposure of 44,933 seconds. The zeroth-order is to “piled” to be useful. (“Pileup” is a term referring to the unresolved temporal coincidence of photons in a 3 × 3 pixel cell, which confounds the accurate determination of the photon energy or gives the wrong pixel pattern. See Davis (2001) for detailed definitions and modeling techniques.)

We use the ephemeris of Berdyugina et al. (1998): the epoch (which defines phase= 0.0) is HJD 2449582.9268, and the period is 6.724333 days. Our observed range of phases is 0.56–0.64. An optical light curve one year later (Tas & Evren 2000) shows the brightness increasing and about mid-way between the maximum and minimum at these phases, with with largest optical brightness modulation ever observed for II Peg. We have not yet seen an optical light-curve contemporaneous with the X-ray observations.

The source varied strongly during the observation. About half-way through the exposure, a flare occurred (see Section 3.3). We separately analyze the pre-flare interval (first 22 ks), the flaring interval (last 17 ks), and also the entire observation.

2.3. Data Processing

Event lists were processed with several versions of the CIAO (Chandra Interactive Analysis of Observations) software suite. The pipeline standard processing used version CIAO 1.1. Custom re-processing was done with various versions of the CIAO tools and the calibration database (CALDB), which are ultimately equivalent to CIAO 2.0 and CALDB 2.0. Further analysis prod-

ucts were made with the CIAO tools to filter bad events (based on grade and bad pixels), bin spectra, make light-curves, make two-dimensional images in wavelength and time, and to make responses.

3. Analysis

Analysis of products produced with CIAO tools was performed either with ISIS⁵ (Houck & DeNicola 2000), which was specifically designed for use on Chandra grating data and as an interface to the APED (“Astrophysical Plasma Emission Database”; Smith et al. (1998)), or with custom programs written in *IDL* (“Interactive Data Language”) using the ISIS measurements and APED emissivities. We used APED version 1.01 in conjunction with the Solar abundances values of Anders and Grevesse (1989) and the ionization balance of Mazzotta et al. (1998).

3.1. Line Fluxes

We measured line fluxes in ISIS by fitting emission lines with a polynomial plus delta-function model convolved by the instrument response. Plus and minus first orders from HEG and MEG were fit simultaneously. Regions of very low counts were grouped by two to four bins from the standard-product scales of 0.005 (MEG) or 0.0025 (HEG) Å/bin. The free parameters were the line wavelengths, the continuum level, and the line fluxes. Up to three line components were fit in some blends or groups. The background is low enough to be neglected, being much less than a count per bin per 50 ks. Statistical 68% confidence limits are computed for each free parameter and are converted into equivalent Gaussian dispersions, since they are predominantly symmetric.

The grating response matrices are a convenient encoding of the instrumental line-profile as a function of wavelength. The response was represented by single-Gaussian profiles. A poorer fit in the wings is apparent in the strongest lines, in is most likely due to inaccuracies in determination and parameterization of the true profile. This does not significantly affect the flux measurements.

The overall effective area calibration is generally accurate to better than 10%, but has some

systematic uncertainties between the different ACIS-S CCDs amounting to about 20% in some regions. The absolute wavelength scale calibration is accurate to about 50-100 km s⁻¹, which allows unambiguous line identification.

We list the line fluxes, statistical uncertainties, and identifications in Table 1. The full spectrum is shown in Figure 1.

3.2. Differential Emission Measure and Abundances

The flux which we determine is an integral over the emitting plasma volume along the line of sight. The plasma could have a range of temperatures, densities, velocities, geometric structures, or non-equilibrium states. We assume it is in Collisional Ionization Equilibrium (CIE). This is not synonymous with thermodynamic equilibrium in which every process is in detailed balance with its inverse. It instead refers to a stable ionization state of a thermal plasma under the *coronal approximation*, in which the dominant processes are collisional excitation and ionization from the ground state, and radiative and dielectronic recombination. In other words, photoexcitation and photoionization are not important, nor are collisional excitation or ionization from excited states. (See McCray (1987) for a good tutorial on thermal plasma processes.) The latter assumption is not strictly true, since there are some lines which are density sensitive through metastable levels, most notably, the helium-like forbidden and intersystem transitions. We treat these separately.

We expect that CIE holds through most of the observation, even though a moderate size flare occurred. If the plasma can ionize or recombine quickly enough relative to an integration time, then we will see some average steady state ionization. Some characteristic times for line appearance through ionization or recombination are given by Golub, Hartquist, & Quillen (1989) in their Table V (columns τ_{app} and τ_{recom}). Most features respond in seconds to hundreds of seconds. The main exception is Mg X in the extended corona and polar plumes, which are low density structures. Mewe et al. (1985) and Doschek, Feldman, and Kreplin (1980) also discuss transient ionization affects in Solar flares.

In our analysis, we did split the spectrum into

⁵ISIS is available from <http://space.mit.edu/CXC/ISIS>

pre-flare and flare states, omitting the time of rapidly increasing flux to provide some insurance against assumption of inappropriate models during a heating phase, in addition to measurement on the spectrum integrated over the entire observation.

We stress, however, that CIE is primarily an assumption. Conditions on stars may not be similar to the Sun in density and energy input profiles. We will assume CIE until we can demonstrate that it fails as a model.

The emitted flux can be expressed as (*cf.* equations 1 and 3 in Griffiths and Jordan (1998))

$$f_l = \frac{A_l}{4\pi d^2} \int dV G_l(T_e, n_e) n_e n_H. \quad (1)$$

The flux in feature l is f_l , A_l is the elemental abundance, d is distance, n_e , n_h are electron and hydrogen densities, V the volume, G_l , is the feature emissivity (in units of photons $\text{cm}^3 \text{s}^{-1}$), and is a function of electron temperature, T_e , and electron density. This formulation also requires that the coronal approximation be valid: that the plasma is optically thin and in collisional equilibrium. The function G contains all the fundamental atomic data as well as an ionization balance. This expression is often approximated by using a mean value of G , since it is typically sharply peaked over a small temperature range. We can write

$$f_l = \frac{A_l}{4\pi d^2} \bar{G}_l E(T_{\max}). \quad (2)$$

\bar{G} is a mean emissivity over the temperature range of maximum emissivity, and E is defined as the “volume emission measure”, or VEM at the temperature of maximum emissivity, T_{\max} . Dependence on n_e has been ignored; many emission lines are only very weakly dependent upon n_e in the expected coronal temperature and density regimes.

It is often more useful to transform the emission measure to a differential form in $\log T$, by restating the volume element, dV , as a function of temperature, $dV(T)$. We then substitute $dV = (dV/d\log T) d\log T$ to derive the form

$$f_l = \frac{A_l}{4\pi d^2} \int d\log T G_l(T) \left[n_e n_h \frac{dV}{d\log T} \right]. \quad (3)$$

The quantity in square brackets is the “differential emission measure” (DEM), which we denote by $D(T)$.

The emission measure is a fundamental quantity of the plasma to be determined, since it represents the underlying balance between the input heating and the energy losses. The integral relation for D cannot be inverted uniquely, given the physical form of G . The functions, $G_l(T)$, are effectively a set of basis functions, but they largely overlap and they are not orthogonal. The mathematics of this equation in the astrophysical context has been studied by Craig & Brown (1976), Hubeny and Judge (1995), and McIntosh et al. (1998). Inversion is possible, but regularization is required to obtain a meaningful solution.

We have adopted a simple χ^2 technique to determine the DEM, and we minimize a discrete form of Equation 3:

$$\chi^2 = \sum_{l=1}^L \frac{1}{\sigma_l^2} \left[f_l - A_{Z(l)} \frac{\Delta \log T}{4\pi d^2} \sum_{t=1}^N G_{lt} \Psi(e^{\ln D_t}, k) \right]^2 \quad (4)$$

Here, l is a spectral feature index, and t is the temperature index. The measured quantities are the f_l , with uncertainties σ_l . The *a priori* given information are the emissivities, G_{lt} , and the source distance, d . The minimization provides a solution for D_t and A_Z . The exponentiation of $\ln D$ forces D_t to be non-negative, and Ψ is a smoothing operator. A_Z is the abundance of element Z . We omit spectral features which are line blends of different elements and of comparable strengths. We use a temperature grid of 60 points spaced by 0.05 in $\log T$, from $\log T = 5.5$ to 8.5. For the initial values of the DEM, we applied Equation 2.

In order to get convergent fits, we need to include as many lines as possible to span a broad temperature range. The fit is not constrained where emissivities go to zero, so filling in the gaps with any available lines is crucial. For this reason, the relative abundances must be included as model parameters. The solution determines relative abundances and a temperature distribution, but has an arbitrary normalization. We remove this degeneracy by examining line-to-continuum ratios. We scale the DEM so that the model continuum agrees with the data, and then scale the abundances inversely. We use a strong feature near the maximum sensitivity, specifically, Mg XI at 9.2Å.

We assess uncertainties in the fit by running simulations with different trial DEM distributions,

from flat to sharply peaked. The input DEM is used to generate line fluxes to which noise is added, and which were then re-fit. We find that peaks in the trial DEM are determined to 0.1 in $\log T$ of the true position, and the fitted distribution does follow the model, with a mean deviation of about 20%. Single sharp peaks are reproduced, with a minimum width (FWHM) of about 0.15 in $\log T$. We also explored variations in the input abundances of our trial models. The fitted abundances reproduce the input values to an accuracy of 20%.

3.3. Light Curves

We made light curves in line and continuum band-passes by binning events from the default extraction regions, including diffracted orders -3 to $+3$ (first orders contain all but a few percent of the counts) and both HEG and MEG spectra. To convert rates to fluxes, we used mean effective areas for the entire observation, since our time bins are large with respect to the dither period (lines bands), or band-passes are large relative to non-uniformities (continuum bands). Figure 2 shows the count-rate integrated over the entire bandpass (1–25 Å), and the flux for a narrower continuum band and for selected lines. Line flux curves are net flux, less a local continuum rate scaled to the line’s bandpass.

4. Results

4.1. Temperature Structure

Figure 3 shows our DEM fits as smooth curves filled with gray shading; the quiescent state is medium gray, the flare state is light gray, and the fit to the entire observation has the darkest shading. The wiggles in the thick outline curves and the deviations between them between $\log T = 6.5$ to 7.3 are characteristic of the uncertainties in the data and models and are not significant. We see two components in the temperature structure. Before the flare, the DEM rises gradually from a very low emissivity below $\log T = 6.5$ to a peak of about 10^{54} near $\log T = 7.2$, then gradually declines, becoming negligible above $\log T = 7.9$. During the flare, a hot component (from about $\log T = 7.3$ to 8.0) is present with a peak value of about four times the maximum quiescent DEM. The lower temperature region is largely unchanged by the

flare. This behavior implies that the flare added a discrete source of emission, and that the cooler source was constant. The fit for the total exposure lies between the two extremes, as it should for a time-weighted average of flare and non-flare line fluxes. The addition of a hot component to the DEM with a relatively unchanged cool component is a common characteristic for flares on RS CVn stars. Mewe et al. (1997) analyzed a flare on II Peg seen with ASCA, and found that the flare contribution could be characterized by the addition of a single hot component. Güdel et al. (1999) concluded that the cool DEM in UX Ari was constant during a flare. Osten et al. (2000) noted a slight enhancement in the cool plasma during a flare onset in σ^2 CrB, which otherwise maintained a constant level of emission.

We compare our emission measure with that derived by Griffiths and Jordan (1998), based on EUVE spectra. We need to apply two scaling factors. First, HIPPARCOS significantly revised the distance determination to II Peg from 29 pc to 42 pc (Perryman & ESA 1997). Second, Griffiths and Jordan (1998) assumed Solar abundances, but the EUVE spectrum is dominated by iron lines. Since the iron abundance is in fact much below Solar (see below), their emission measure must be scaled accordingly. Applying these factors, we find that their emission measure approximately follows our mean curve, except for the large peak at $\log T = 6.8$, as is shown in Figure 3.

Mewe et al. (1997) fit emission measure distributions to EUVE and ASCA spectra, which we over-plot on Figure 3. Their structure appears more peaked than ours. While their flare DEM (the peak at highest $\log T$) is comparable to ours, the lower temperature structure is very different. Integrated values are similar.

The high temperature fit region is primarily determined by high ionization states of Fe, S, Si, and Ar. The lower ionization states of iron (XVII-XXI) do not change much during the flare, but lines from Fe XXII-XXV increased significantly. Other ions, such as O VIII and Ne X, whose emissivities peak at relatively low temperatures ($\log T = 6.5 - 6.8$) but also have extremely long tails to very high temperature, also increased in strength. Figure 4 shows the flux modulation between flare and quiescent states. The modulation is defined as the ratio of the flux difference to the flux sum

for flare and quiescence. For no change, the modulation is 0.0, and for 100% change, 1.0 (in the sense of flare minus quiescent). We grouped lines by $\log T_{\max}$ to form mean fluxes before computing the modulation. The increase in modulation with T_{\max} is clear. In particular, note that Fe XXV ($\log T_{\max} = 7.7$) is not detected in the pre-flare state, Fe XXIV ($\log T_{\max} = 7.3$) changed appreciably, but Fe XVII ($\log T_{\max} = 6.7$) lines change little. To explicitly quantify the changes for some lines, we tabulate pre-flare and flare fluxes in Table 2. The values tabulated are representative of the modulations plotted, but are not precisely the same line groups, so actual values will differ slightly from those plotted.

The continuum can also be used to constrain the temperature distribution. In Equation 3, $G(T)$ in this respect is the continuum emissivity integrated over a given bandpass. Given the form of the continuum emissivity and its slow variation with temperature, the solution is not unique: the same flux could be obtained from a flat or sharply peaked emission measure distribution. Fitting the continuum in the same way as line fluxes is not practical. Instead, continuum-band flux ratios can be used to estimate temperatures, assuming that emission is dominated by a single temperature. We use the flux ratio of a 2–6 Å band to the 7–8 Å band from the APED model continua, and compare the theoretical ratios to observed ratios in flare and non-flare states. The ratio clearly changes, and is consistent with the DEM fits, indicating a change from $\log T$ of 7.3 to 7.6 between quiescent and flare states. This is not a unique result: using a longer wavelength band of 10–12 Å, for example, systematically shifts derived temperatures to lower values. Continuum bands are thus qualitatively useful, but cannot easily quantify the temperature distribution.

We computed a continuum modulation between flare and quiescent states similarly to line fluxes. The continuum fluxes were taken from the line plus continuum fits, and for a characteristic $\log T$, we computed a pseudo-temperature for each wavelength ($T = hc/k\lambda$). This is a crude parameterization of the temperature dependence of the shortest wavelength continuum contribution, since higher temperatures lead to stronger short-wavelength continuum. The continuum modulation is shown on Figure 4. It increases very weakly to higher

temperature, with a mean value of about 0.5, which means that the flare state had about three times the continuum flux as the quiescent state.

The log integrated emission measures are 53.9 and 54.3 (for volume in cm^{-3}) for the quiescent and flare states, respectively. The corresponding observed fluxes and luminosities for the 1–25 Å wavelength range are 0.52 and $1.3 \times 10^{-10} \text{ ergs cm}^{-2} \text{ s}^{-1}$, and 1.1 and $2.9 \times 10^{31} \text{ ergs s}^{-1}$, respectively. These luminosities are comparable to those obtained by Covino et al. (2000) but about twice times that of Mewe et al. (1997) (after the latter were scaled to the revised distance of 42 pc, a factor of two in luminosity).

4.2. Elemental Abundances

Relative elemental abundances are crucial to the fit of a DEM to line fluxes. Absolute abundances relative to hydrogen can be deduced by adjusting the line-to-continuum ratio. The values we obtain are given in Table 3. The uncertainties are determined by *ad hoc* perturbation of an abundance, generating a model spectrum, and comparing it to the observed spectrum. For the stronger lines (Ne, O), a change of 10–15% could be easily detected. For elements with only weak lines, such as Ar XVII or S XV, the uncertainties are as large as a factor of two.

We also performed trial runs of the abundance fitting of line fluxes as we did for the temperature distribution. For several trial DEM distributions, we assumed a set of trial abundances, evaluated model line fluxes, introduced noise, and then fit to derive the DEM and abundances. Variances in the derived trial abundances are consistent with the above subjective inspection of models

Iron is extremely underabundant, at about 0.15 times Solar (-0.8 dex). Neon is overabundant by about a factor of two. Ottmann, Pfeiffer & Gehren (1998) modeled the photospheric lines of iron, magnesium, and silicon in II Peg. Their abundances relative to Solar were about 0.6, 0.7, and 0.7, respectively (-0.22, -0.15, and -0.15 dex). Berdyugina et al. (1998) determined a comparable photospheric metallicity of 0.3–0.5 times Solar. Our coronal abundance for iron is about four times lower, while Mg and Si are within 70% of their values and are within our respective uncertainties. Mewe et al. (1997) fit EUVE and ASCA spectra

of II Peg, and they required variable, non-Solar abundances. Our iron abundances are comparable, but values for other species differ by about a factor of 3–4, though the neon to oxygen ratio is similar. The differences are probably due to uncertainties in spectral fitting to the previous low-resolution data.

The DEM fit gives neon to iron ratios relative to the Solar ratio of 22 ± 6 (pre-flare) to 17 ± 5 (flare) or 16 ± 4 (total spectrum). Fe XVII and Ne IX have nearly identical theoretical emissivity profiles: they are both sharply peaked, and their temperatures of maximum emissivity are separated by less than 0.1 in $\log T$. Hence, the flux ratios of Fe XVII to Ne IX should only depend upon their relative abundances and atomic parameters. We compared flux ratios of Ne IX 13.446 Å resonance line, since it is relatively unblended, to the Fe XVII line at 15.01. The flux ratios and APED emissivities imply that the neon to iron abundance ratio (for the total spectrum) is 14 ± 2 times the Solar ratio. For the pre-flare and flare intervals, respectively, we obtain the ratios 14 ± 4 and 16 ± 5 . The line-ratio and DEM values are all identical, given the statistical uncertainties.

4.3. Densities

The helium-like triplets of O VII, Ne IX, Mg XI, and Si XIII which are detected and resolved into the resonance (*r*), intercombination (*i*), and forbidden (*f*) lines by the HETGS. These lines are useful because the flux ratio of *f*/*i* is primarily density-sensitive, and (*f* + *i*)/*r* is mainly temperature sensitive (Gabriel and Jordan 1969; Pradhan 1982; Porquet & Dubau 2000). The ratios are not dependent upon the ionization balance since they are from the same ion, and since they are close together in wavelength they are relatively insensitive to calibration uncertainties. The critical density, above which the ratio, *f*/*i*, drops from a nearly constant, low-density limit, rises by about a decade for each of O VII, Ne IX, Mg XI, to Si XIII, starting near 10^{10}cm^{-3} for oxygen to 10^{13}cm^{-3} for Si, spanning an interesting range of expected coronal densities. The He-like triplets of S XV, Ca XIX, Ar XVII, and Fe XV lines are also in the HETGS band, but are either weak or unresolved. Their critical densities are also well above the coronal range.

We have determined the limits in density im-

plied by the APED models for our measured line fluxes. Since the lines did not change substantially during the flare, we used the flux integrated over the entire observation to achieve the best signal. We also only consider temperatures near the peak emissivity times emission measure, which limits the range to roughly $\log T$ 6.0–7.0 for O VII, Ne IX, and Mg XI. The 68% confidence limits in $\log N_e$ for oxygen are 10.6–11.6 [$\log \text{cm}^{-3}$]. Ne IX gives 11.0–12.0, with a barely constrained lower limit. The range for Mg XI is 12.8–13.8. The respective 90% limits for O VII, Ne IX, and Mg XI are 10.3–12.4, < 12.3 , and > 11.8 . Si XIII density is unconstrained.

The neon and oxygen density limits overlap, while magnesium and neon are marginally inconsistent. There are plausible systematic affects, such as line blends and continuum placement. The Ne IX intersystem line (13.55 Å) is blended with Fe XIX (13.52 Å), but two peaks are resolved and are easily fit with two components. Unaccounted blends in the Mg XI *i* could lower the measured *f*/*i* ratio resulting in an erroneously higher density. The observed Mg XI *i* flux is significantly greater than the predicted model (see Figure 5b, 9.23Åregion).

We believe the discrepancy is caused by blending of the Ne x Lyman series with the Mg XI lines. Levels above $n = 5$ are not included in the APED models, and they are probably responsible for the clear excess of data over prediction in the 9.2–9.5 Å range. In particular, the Ne x Lyman series lines from upper levels 6–10 fall at 9.362, 9.291, 9.246, 9.215, and 9.194 Å. These will have to be included in models if we are to obtain reliable Mg XI triplet ratios, especially in stars with enhanced neon abundance.

An increase in the Mg XI *f*/*i* ratio by about 50% would put the density lower-limit at about 12.3, while doubling the ratio would make the lower-limit unconstrained. It is difficult to reconcile densities between Mg and O without a factor of two error in the Mg ratio; given the model uncertainties and the difficulty of fitting the blends, such an error is likely.

For two-sigma confidence intervals, O, Mg, and Ne together imply consistent logarithmic density near 11.8–12.3. However, there is no *a priori* reason to expect density to be constant with temperature, and hence the same for each ion.

4.4. Resonant Scattering

The ratio of the Fe XVII $\lambda 15.265$ ($2p^6 1S_0 - 2p^5 3d^3 D_1$) to its resonance line neighbor at $\lambda 15.014$ (upper level $2p^5 3d^1 P_1$) is a measure of density and geometry, since the latter has a shorter mean free path. Saba et al. (1999) have summarized Solar measurements and theoretical values for the ratio and concluded that opacity is a factor in the Sun; theoretical calculations and Solar measurements give ratios of 0.25 ± 0.04 and 0.49 ± 0.05 , respectively. Recent laboratory measurements obtained values in the range 0.33 ± 0.01 (Brown, et al. 1998). Laming et al. (2000) measured these as well as the nearby 17 \AA lines sharing the same lower level, and compared to theory. Their observed ratio was 0.40 ± 0.02 , and the ratio of the 17 \AA pair to the resonance line at 15 \AA was 0.9 ± 0.1 , for a beam energy of 1.25 keV . Both Brown and Laming et al. suggested that opacity effects in the Sun have been overestimated, since the improved measurements have raised the ratios towards the Solar values, and because there are physical processes other than collisional excitation and radiative decay which have not yet been accounted for in the theoretical calculations.

We have measured a 15.26 to 15.01 flux ratio of 0.48 ± 0.14 in the HETGS spectra, which is as large as the Solar values, and larger than the value of 0.26 ± 0.1 determined for Capella (Brinkman et al. 2000; Canizares et al. 2000). The uncertainty, however, is large enough that the result is not inconsistent with the other values. We see no direct evidence of opacity in Fe XVII in II Peg.

Our ratios of the 17 \AA lines to the 15 \AA line is 2.1 ± 0.4 , which is twice the laboratory value of 0.9 ± 0.1 . This ratio is weakly temperature dependent; the APED ratio ranges from 0.8 at $\log T = 7.2$ to 1.3 at 6.1 . There is some systematic incurred in our measured value from continuum placement, but not a factor of two. If we had used these lines for our relative neon-to-iron abundance determination, we would have obtained a value a factor of two lower. (The lines were used implicitly in the DEM fitting, but their affect is diluted by the presence of other lines of Fe.) Laming et al. (2000) discuss some possibilities for “small” contributions to the upper levels which produce the 17 \AA lines, such as recombination from Fe XVIII into excited levels, but none can explain the large

discrepancy between various Solar and stellar observations, which they show in their Figure 3. We have neither an atomic nor plasma physics explanation for the anomalous relative strength of Fe XVII 17 \AA lines.

We have also looked at the ratios of the Ly- α -like series for O VIII, Ne X, and Si XIV. None differ significantly from the APED theoretical ratios. The largest difference is for O VIII; the $\beta : \alpha$ ratio of 0.19 ± 0.015 (68% confidence) and the theoretical value is 0.16 . Hence, we have no direct evidence of scattering in O VIII Ly- α . The ratio is not affected by interstellar absorption, since the column density required to change the $\beta : \alpha$ to exactly match the theoretical value would make II Peg invisible to EUVE. Estimates have been made from EUVE spectra of a few times 10^{18} cm^{-2} (Griffiths and Jordan 1998), which we will adopt. This amount has negligible affect on the X-ray spectrum. None of the Ly-series ratios for oxygen or neon changed significantly during the flare.

4.5. Line Profiles and Shifts

Line shifts and shapes can be important diagnostics of plasma dynamics. Flares may have upflows or downflows of up to 400 km s^{-1} , which would be resolvable by HETGS. However, we observe the flare emission against the background quiescent emission, and the flare emission was predominantly in the continuum, though lines did increase somewhat in flux. We did not see any significant line shifts during the flare, which we inspected by differencing the pre-flare spectrum from the flare spectrum. Small shifts would show as differential profiles, but we only saw the small change in line flux.

Line shapes are more difficult to assess, especially if broadening is comparable to the instrumental resolution. A very good calibration of the instrumental profile is needed. Profile fits suggest that O VIII 19 \AA is slightly broader than instrumental, but we are not yet confident enough on the calibration of the intrinsic profile at this level. The calibration is being improved, and we will apply it when available.

5. Discussion

5.1. Abundances and Temperature Structure

There has been much discussion and controversy regarding low metal abundances in stellar coronae. Previous low-resolution investigations found reduced abundances of some elements, such as for UX Ari (Güdel et al. 1999), σ^2 CrB (Osten et al. 2000), and II Peg (Mewe et al. 1997). (Also see reviews by White et al. 1996; Pallavicini et al. 1999). Without being able to resolve individual lines, counter-arguments have criticized over-simplistic emission measure models which fit only two temperature components, limitations of emissivity models in which a pseudo-continuum from many weak lines would artificially reduce line-to-continuum ratios, enhanced helium abundance leading to stronger continuum (Drake 1998), ignorance of photospheric abundances, or calibration uncertainties. Drake (1996) applied the term, “MAD” (for Metal Abundance Deficient) for the low-abundance objects. Much of the interest in abundances has been driven by empirical evidence of the “First Ionization Potential” (FIP) affect in the Sun (Feldman, Widing, & Lund 1990; Laming, Drake, & Widing 1996) in which easily ionized elements are over-abundant in the corona. This is generally the opposite of what is inferred in other stars: the FIP affect enhances iron in the Solar corona relative to other elements. Feldman & Laming (2000) give a thorough review of the state of abundance determinations in the coronae of the Sun and other stars.

With Chandra spectra, we are now able to settle some of these questions. Drake et al. (2001) have found neon to be much enhanced relative to iron in HR 1099. II Peg is similar: it is clearly deficient in iron, and neon is enhanced. This is not a simple reflection of the photospheric abundances.

While we have improved the quality of abundance determinations in II Peg, we cannot explain them. II Peg is somewhat MAD, but has high neon. It definitely does not show the FIP affect, but much the opposite (we tabulate the FIP in Table 3). The iron deficiency is quite strong, and there are large discrepancies between some observed ratios and the theoretical or laboratory values. Brinkman et al. (2001) reported an inverse FIP affect in HR 1099 as determined

from XMM-Newton Reflection Grating Spectrometer data. From HETGS spectra of HR 1099, Drake et al. (2001) determined abundances similar to Brinkman’s values. Neither HR 1099 nor II Peg show a truly uniform FIP affect. At the lowest ionization potentials, there is a factor of several spread between the low Fe and moderate Mg and Si abundances.

Our preliminary work on other stars with HETGS spectra hints that there is a range of iron abundance from very low in II Peg, to moderate depletion AR Lac and TY Pyx, which seem to have higher Fe/Ne abundance ratio than HR 1099. Capella appears to be at the “normal” end of the distribution, with neither strong iron nor neon deviations from cosmic abundances (Audard et al. 2001).

The temperature structure we obtain is much different from previous DEM determinations. Ours is much smoother. While some smoothing has been imposed to make the fit better behaved, we should have been able to resolve features as sharp as found by Griffiths and Jordan (1998) and Mewe et al. (1997). Our simulations showed that we could fit peaks with $FWHM \sim 0.15$ dex in $\log T$. We suspect that the improved resolution and spectral coverage spanning a greater range in ionization states and elements are key factors. Further studies are required to determine the affects of fitting methods, spectral resolution, and range of model space provided by spectral features on resulting DEM distributions.

5.2. Flare Models

It is possible to model flare light-curves to derive constraints on the loop sizes, magnetic fields, and densities. Kopp and Poletto (1984) have formulated a model for two-ribbon flares based on detailed Solar observations, which Poletto et al. (1988) extended to other stars. Their model describes the conversion of magnetic energy to X-rays via reconnection of rising loops, assuming the flare occurs at the site of reconnection at the top of the rising loops. This model has been frequently applied to ultraviolet and X-ray flares on RS CVn stars (Güdel et al. 1999; Osten et al. 2000). A complementary approach can be found in van den Oord et al. (1988) and subsequent papers (e.g. van den Oord & Mewe 1989; van den Oord et al. 1997), including application to II Peg (Mewe et al. 1997),

in which conductive and radiative energy balance are applied to the flux and temperature profiles.

There are a large number of parameters in these models, some poorly constrained, such as the fraction of energy emitted in X-rays, the magnetic field, the number of loops, the shape of loops, and the electron density. The observable quantities are the shape of the light-curve, the light-curve amplitude, and the spectrum of the plasma. The models are most constrained by the decay phase under the assumption that heating has stopped. Even this simplification is suspect, however, since flare light-curves have shown extremely long or structured decay (Osten et al. 2000).

We do not observe enough of the flare decay in this observation to determine two of the fundamental parameters in the Kopp & Poletto model: the loop size, and the time constant. The decay function (see equations 2–6 in Güdel et al. 1999) differs most for different loop sizes at about 50 ks into the flare, whereas we have observed only about 25 ks. We did not observe enough of the decay to determine a cooling profile from the spectrum. There is no density diagnostic available in the net flare spectrum above the constant background coronal emission. Better diagnostics will come when a very large flare is observed over the right time interval, which is bright enough to measure density diagnostics in spectral lines.

We have compared the two-ribbon reconnection model energy profile to the light-curve we have. The smooth line plotted in Figure 2 shows the arbitrarily normalized model for a time-constant of 65 ks and a point-like flare. The top portion of the figure shows the counts integrated over all diffracted photons, while the bottom shows a narrow band from 6.8–8.2 Å. The normalization factor for the latter requires about a 20% relative difference from the broad-band curve, indicating that there is perhaps some chance of constraining the model with continuum band information. We will pursue low-resolution light curve quantitative flare diagnostics in future work.

The time-constant is not a characteristic cooling time, nor the exponential decay constant, but is the Kopp & Poletto reconnection time scale parameter related to loop dynamics and continuous heating. If we had more of the decay profile, we might be able to assess the relative affects of continuous heating (reconnection), or whether the

probably long decay is due to less efficient conductive and radiative cooling due to larger, lower density structures than seen on the Sun. Golub, Hartquist, & Quillen (1989) list some characteristic cooling times for different density structures (their Table V), which span several orders of magnitude from 500 to 10^5 seconds. Hence, it is possible to have long-lived flares without continuous heating if densities are low.

We do not see any evidence of impulsive behavior before the obvious flare onset at about 24 ks, but this could be easily masked by the background quiescent emission. Impulsive events are also likely to be harder than the response range of the HETGS, since these precursor flares are characterized by rapid variability at energies greater than 20 keV.

There is a hint that Ne and Fe are enhanced during the flare (see Table 3), but it is $\leq 2\sigma$ affect, and not conclusive that flare abundance variations occur in II Peg, as they do in the Sun.

5.3. Loop Sizes

Given our emission measure determination and density estimates, we estimate loop sizes under the simplifying assumption of uniform cross section, semicircular loops intersecting a plane (a hemitoroidal loops). We define L as the loop length from foot point to foot point along the loop axis, and h as the height defined from the midpoint of the segment connecting the centers of the circular bases to the center of the loop cross-section (i.e., the radius of the axis of the loop). Thus, $L = \pi h$. We define α as the ratio of the loop cross-sectional radius to the loop length. The loop volume is then $V = \pi^4 \alpha^2 h^3$. Noting that the volume emission measure, VEM , is approximately $N_e^2 V$, we can write the loop height as a function of VEM and N_e in units of the stellar radius, R_* , for an ensemble of identical emitting loops as

$$h = \pi^{-4/3} N_{100}^{-1/3} \alpha_{0.1}^{-2/3} (VEM)^{1/3} n_e^{-2/3} R_*^{-1}, \quad (5)$$

where N_{100} is the number of loops divided by 100 (an arbitrary normalization), and $\alpha_{0.1}$ is the ratio of loop radius to loop length in units of 0.1 (a number typically used for Solar loops).

For our determinations of $VEM = 7.9 \times 10^{53} \text{ cm}^3$ (for quiescent state) and $n_e \sim 10^{11} \text{ cm}^3$, a stellar radius of $3R_\odot$ (Berdyugina et al. 1998),

$N_{100} = 1$, and $\alpha = 1$, we find that $h = 0.05$. The loops are small compared to the stellar radius. If we compute the height for the flare excess VEM and assume a single loop, then it could be 0.25 of the stellar radius for the same density. If flare density were enhanced by a factor of 10, then the loop size remains at 0.05. It may be possible to detect loops of this size in other systems via X-ray light curves of eclipses. We are pursuing such observations.

5.4. Model Spectrum

A final test of any model is a prediction of the observed data, especially observed features which were not used in determination of the model. We use the derived emission measure and abundances for the entire duration of the observation to model a spectrum (using the APED in ISIS) and fold this through the instrumental effective area and line-spread-function. Figures 5a-5d show the counts spectrum and folded model. There are features which are clearly not in the APED database, or have poorly determined wavelengths or emissivities, or where there are larger calibration errors. This comparison does not show that the model is necessarily “correct”, but that it is not inconsistent with the observation. It is actually a very good match, but there are clearly regions where better fits should be pursued, and discrepancies between models and data resolved.

6. Conclusions

II Pegasi is a very interesting and much studied RS CVn star, uncomplicated by a secondary star’s spectrum. We have confirmed that its corona is indeed iron deficient, and deficient relative to the photosphere. We have also shown that neon has a substantially enhanced coronal abundance. Our temperature structure is much smoother than prior studies which does not seem to be an artifact of DEM modeling. A moderate sized flare enhanced the hot component, as evidenced primarily in the continuum. The flare is consistent with a Solar two-ribbon model, but not enough of the decay was observed to provide physical constraints. Loop sizes are fairly small, about 5% of the stellar radius, but this is larger than estimates for Capella (Canizares et al. 2000) and perhaps enough to encourage X-ray light curve studies of

eclipsing systems.

Work at MIT was supported by NASA through the HETG contract NAS8-38249 and through Smithsonian Astrophysical Observatory (SAO) contract SVI-61010 for the Chandra X-ray Center (CXC). We thank all our colleagues who helped develop and calibrate the HETGS and all members of the Chandra team, in particular the CXC programming staff. We especially thank John Houck for his support of ISIS, Dan Dewey for a critical review of the manuscript, and Nancy Brickhouse for providing insight regarding the Mg XI ratios.

REFERENCES

- Anders, E., & Grevesse, N., 1989, *Geochimica et Cosmochimica Acta* 53, 197.
- Audard, M., Behar, E., Güdel, M., Raassen, A. J. J., Porquet, D., Mewe, R., Foley, C. R., & Bromage, G. E. 2001, *A&A*, 365, L329.
- Berdyugina, S. V., Jankov, S., Ilyin, I., Tuominen, I. & Fekel, F. C. 1998, *A&A*, 334, 863
- Brinkman, A. C. et al. 2000, *ApJ*, 530, L111.
- Brinkman, A. C. et al. 2001, *A&A*, 365, L324.
- Brown, G.V., Beiersdorfer, P., Liedahl, D.A., et al., 1998, *ApJ*, 502, 1015.
- Canizares, C. R. et al. 2000, *ApJ*, 539, L41
- Canizares, C.R. et al. 2001 in preparation
- Chugainov P.F., 1976, *Iz. Kry.* 57, 31.
- Covino, S., Tagliaferri, G., Pallavicini, R., Mewe, R. & Poretti, E. 2000, *A&A*, 355, 681
- Craig, I.J.D., and Brown, J.C., 1976, *A&A*, 49, 239
- Davis, J.E., *ApJ*, (submitted).
- Doschek, G.A., Feldman, U., and Kreplin, R.W., 1980, *ApJ*, 239, 725.
- Drake, J.J., *ApJ*, 496, L37.
- Drake, J.U., 1996, in “Cool Stars, Stellar Systems, and the Sun”, Pallavicini, R. and Dupree, A.K. (eds.), *PASP Conf. Series*, 109, 203.
- Drake, J.J., et al., 2001, *ApJ*, 548, L81
- Feldman, U., & Laming, J. M., 2000, *Physica Scripta*, 61, 222.
- Feldman, U., Widing, K. G., & Lund, P. A. 1990, *ApJ*, 364, L21
- Gabriel, A.H., & Jordan, C., 1969 *MNRAS*, 145, 241.
- Golub, L., Hartquist, T. W., & Quillen, A. C. 1989, *Sol. Phys.*, 122, 245
- Griffiths, N.W., & Jordan, C., 1998 *ApJ*, 497, 883
- Güdel, M., Linsky, J.L., Brown, A., Nagase, F., 1999, *ApJ*, 511, 405.
- Houck, J.C., and DeNicola, L.A., 2000, ‘ISIS: An Interactive Spectral Interpretation System for High Resolution X-Ray Spectroscopy”, in *Astronomical Data Analysis Software and Systems IX*, ASP Conf. Ser., Vol 216, (San Francisco: ASP), 591.
- Hubeny, V., Judge, P.G., 1995, *ApJ*, 448, L61
- Kopp, R.A., and Poletto, G., 1984, *Sol. Phys.*, 93, 351
- Laming, J. M. et al. 2000, *ApJ*, 545, L161
- Laming, J. M., Drake, J. J., & Widing, K. G. 1996, *ApJ*, 462, 948
- Markert, T.H., Canizares, C.R., Dewey, D., McGuirk, M., Pak, C.S., & Schattenburg, M.L., 1994, *Proc. SPIE*, 2280, 168.
- McCray, R., in “Spectroscopy of astrophysical plasmas”, A. Dalgarno and D. Layzer, (Cambridge Univ. Press, Cambridge), 1987, p. 255.
- McIntosh, S.W., Brown, J.C., and Judge, P.G., 1998, *A&A*, 333, 333
- Mewe, R., Lemen, J.R., Peres, G., Schrijver, J., and Serio, S., 1985, *A&A*, 152, 229.
- Mewe, R., Kaastra, J. S., van den Oord, G. H. J., Vink, J. & Tawara, Y. 1997, *A&A*, 320, 147
- Mazzotta, P., Mazzitelli, G., Colafrancesco, S., & Vittorio, N. 1998, *A&AS*, 133, 403
- Osten, R.A., Brown, A., Ayres, T.R., Linsky, J.L., Drake, S.A., Gagné, M., Stern, R.A., 2000, *ApJ*, 544, 953.
- Ottmann, R., Pfeiffer, M. J. & Gehren, T. 1998, *A&A*, 338, 661
- Owen, F. N. & Gibson, D. M. 1978, *AJ*, 83, 1488
- Pallavicini, R., Maggio, A., Ortolani, A., Tagliaferri, G., and Covino, S., 1999, *Ap&SS*, 261, 101.
- Perryman, M. A. C. & ESA 1997, “The Hipparcos and Tycho catalogues. Astrometric and photometric star catalogues derived from the ESA Hipparcos Space Astrometry Mission”, *ESA SP Series*, 1200 (Noordwijk, Netherlands: ESA),

- Poletto, G., Pallavicini, R., and Kopp, R.A., 1988, A&A, 201, 93
- Porquet, D. & Dubau, J. 2000, A&AS, 143, 495
- Pradhan, A. K. 1982, ApJ, 263, 497
- Rucinski, S. M. 1977, PASP, 89, 280
- Saba, J.L.R., Schmelz, J.T., Bhatia, A.K., and Strong, K.T., 1999, ApJ, 510, 1064.
- Schwartz, D. A., Garcia, M., Ralph, E., Doxsey, R. E., Johnston, M. D., Lawrence, A., McHardy, I. M. & Pye, J. P. 1981, MNRAS, 196, 95
- Smith, R. K., Brickhouse, N. S., Raymond, J. C., & Liedahl, D. A. 1998, in Proceedings of the First XMM Workshop on “Science with XMM”, ed. M. Dahlem (Noordwijk, The Netherlands)
- Strassmeier, K.G., Hall, D.S., Fekel, F.C., and Scheck, M., 1993, A&AS, 100, 173
- Tas, G. & Evren, S. 2000, Informational Bulletin on Variable Stars, 4992, 1
- van den Oord, G.H.J., & Mewe, R., 1989, A&A, 213, 245
- van den Oord, G.H.J., Mewe, R., & Brinkman, A.C., 1988, A&A, 205, 181
- van den Oord, G.H.J., Schrijver, C.J., Camphens, M., Mewe, R., & Kaastra, J.S., 1997, A&A, 326, 1090
- Walter, F. M. & Bowyer, S. 1981, ApJ, 245, 671
- White, N. E., 1996, in “Cool Stars, Stellar Systems, and the Sun”, Pallavicini, R. and Dupree, A.K. (eds.), PASP Conf. Series, 109, 193.

Fig. 1.— We show the HETGS flux spectrum of II Pegasi. The spectrum is the combined HEG and MEG, diffracted orders -3 to +3. It has been smoothed for presentation. Some prominent lines have been labeled.

Fig. 2.— The top panel shows the full-band count-rate light curve. The smooth curve is a two-ribbon Solar flare model. The bottom shows the continuum light curve in a narrow, short-wavelength bandpass. Symbols show the light curve in net line fluxes for a few features. Note the decreased amplitude of the lines, relative to the continuum.

Fig. 3.— We show the model of the differential emission measure for the flare, quiescent, and total spectrum. Differences in the fit from $\log T = 6.5 - 7.2$ are indicative of uncertainties in the fitting. The large, hot peak is the flare, which did not affect the cooler region of the DEM. Overplotted points, connected with broken lines, are the DEM determinations of Griffiths and Jordan (1998) and Mewe et al. (1997).

Fig. 4.— We show the modulation of line and continuum between flare and quiescent states. The modulation is defined as $[f(flare) - f(quiescent)]/[f(flare) + f(quiescent)]$. It is 1.0 for $f(quiescent) = 0$, and 0.0 for $f(quiescent) = f(flare)$. Lines have been grouped by $\log T_{\max}$, and clearly show increasing modulation with temperature, meaning that the flare was very hot. Features which give a better than 2.5σ confidence in the modulation have been emphasized.

The continuum modulation is defined similarly, except that T_{\max} is not well defined. Instead, we use a pseudo-temperature derived from the continuum band wavelength ($T = hc/k\lambda$), primarily to enable placement of continuum data on the same axis. The continuum is strongly modulated with about equal amplitude in each wavelength band. It is not very sensitive to temperature because its emissivity distribution is broad — a hot continuum adds significant flux at all wavelengths above a lower limit (or, at all lower pseudo-temperatures).

Fig. 5.— Panels a-d show detailed comparison of the observed counts spectrum and the model folded through the instrumental response. This is the spectrum for the entire observation and uses

the fitted DEM and abundances. The spectra have been smoothed by a Gaussian kernel with width equal to the instrument resolution (0.008\AA and 0.004\AA Gaussian σ 's for MEG and HEG, respectively). The spectra were binned to 0.005\AA (MEG) and 0.0025\AA (HEG). The upper curves are MEG counts, and the lower HEG. The dotted curve is the model. Up to eight of the brightest features in the APED emissivity tables for the given model have been labeled in each graph.

Fig. 5b.— See 5a.

Fig. 5c.— See 5a.

Fig. 5d.— See 5a.

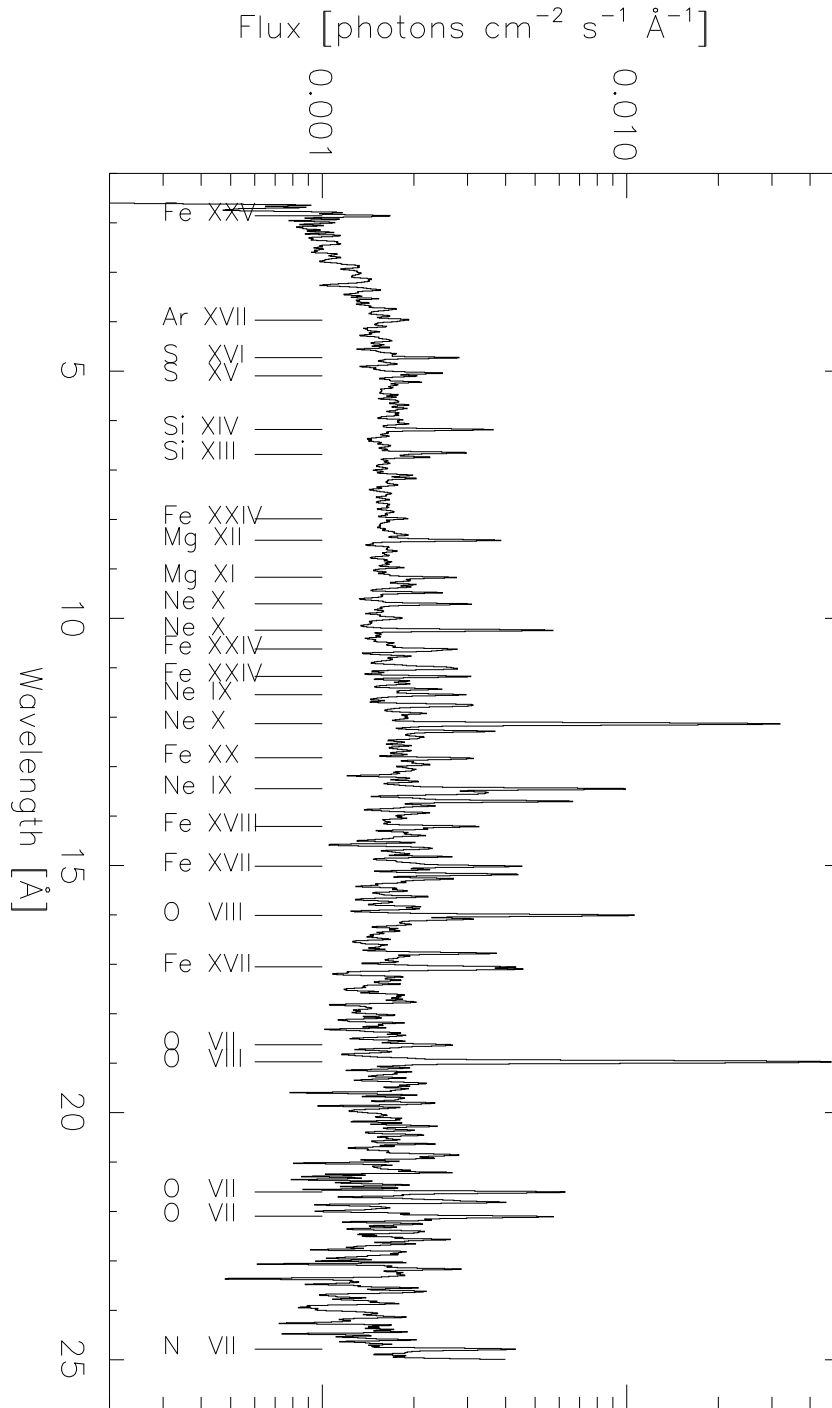


Fig. 1.— We show the HETGS flux spectrum of II Pegasi. The spectrum is the combined HEG and MEG, diffracted orders -3 to +3. It has been smoothed for presentation. Some prominent lines have been labeled.

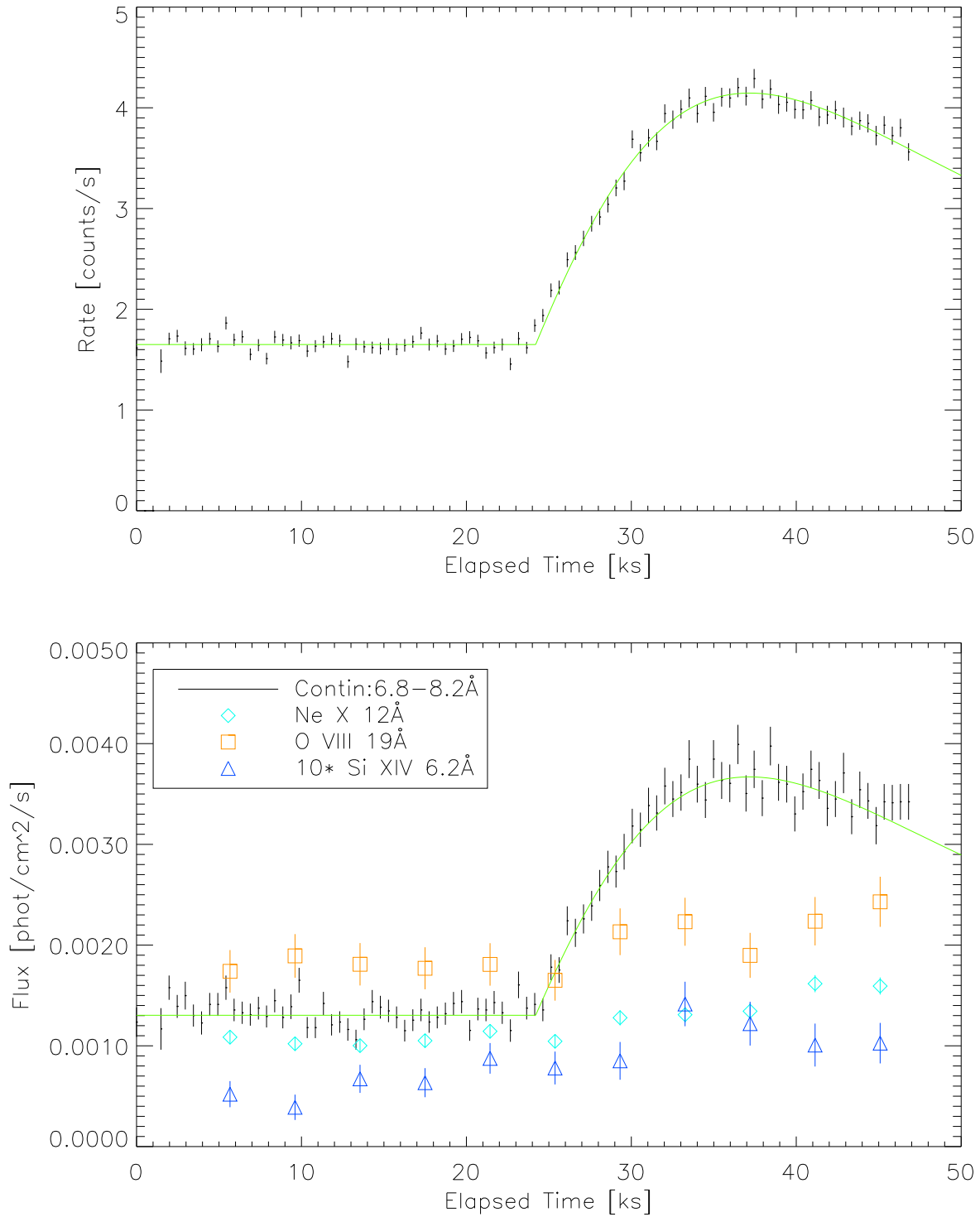


Fig. 2.— The top panel shows the full-band count-rate light curve. The smooth curve is a two-ribbon Solar flare model. The bottom shows the continuum light curve in a narrow, short-wavelength bandpass. Symbols show the light curve in net line fluxes for a few features. Note the decreased amplitude of the lines, relative to the continuum.

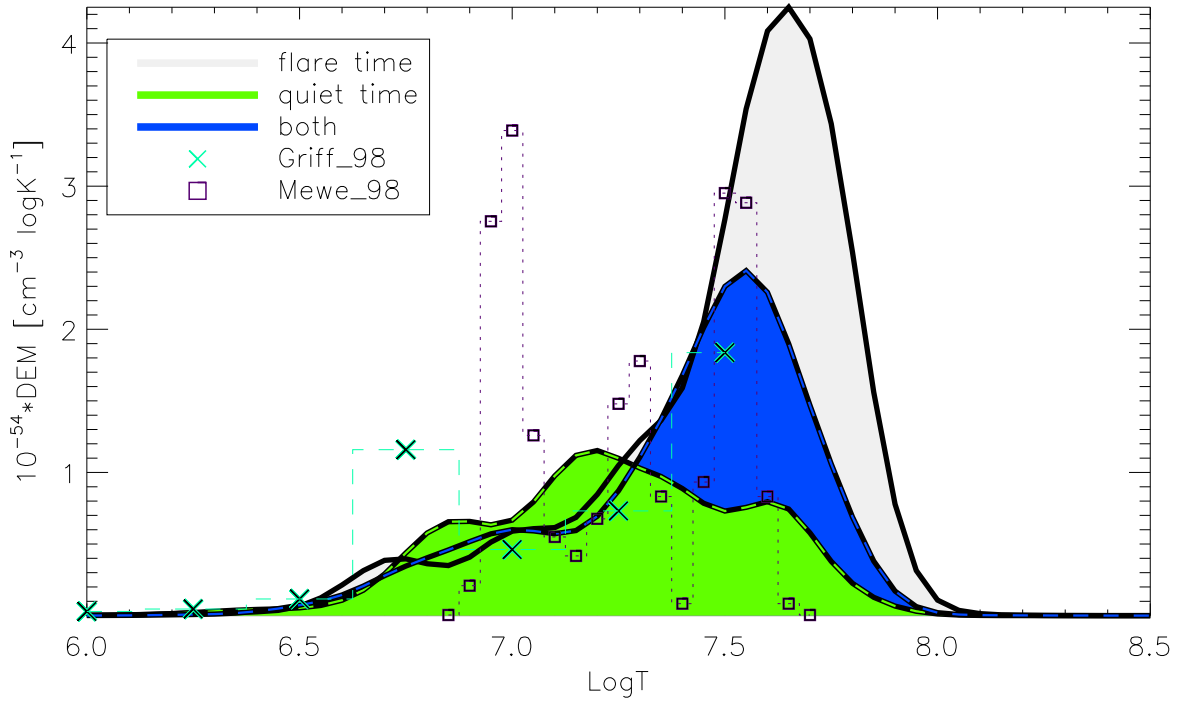


Fig. 3.— We show the model of the differential emission measure for the flare, quiescent, and total spectrum. Differences in the fit from $\log T = 6.5 - 7.2$ are indicative of uncertainties in the fitting. The large, hot peak is the flare, which did not affect the cooler region of the DEM. Overplotted points, connected with broken lines, are the DEM determinations of Griffiths and Jordan (1998) and Mewe et al. (1997).

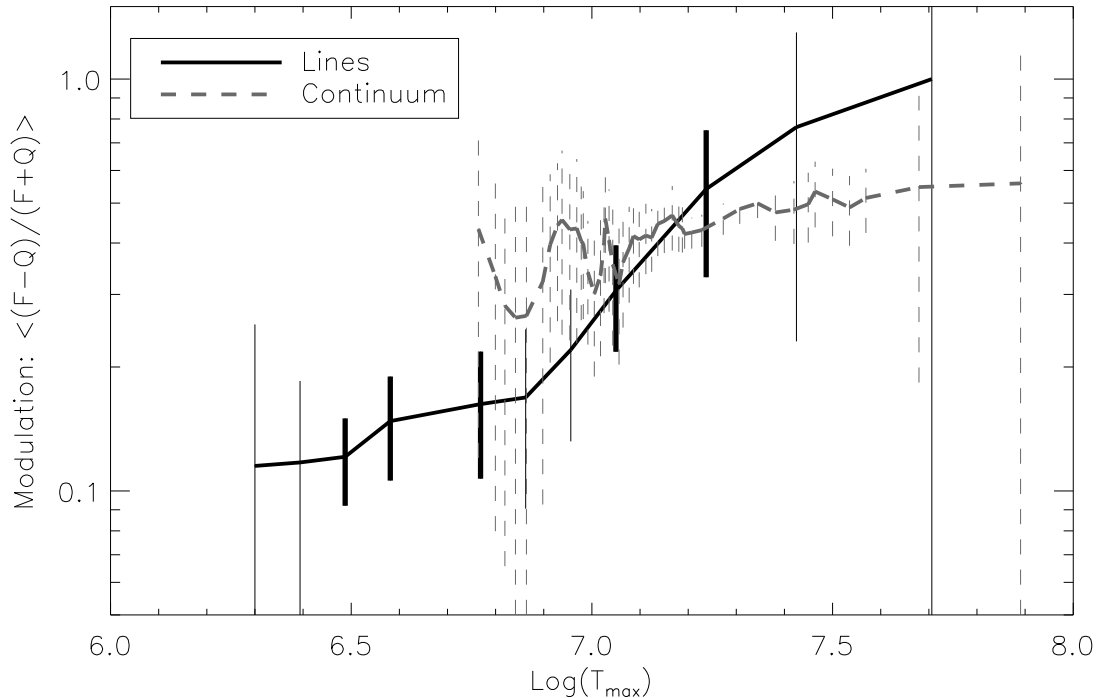


Fig. 4.— We show the modulation of line and continuum between flare and quiescent states. The modulation is defined as $[f(\text{flare}) - f(\text{quiescent})]/[f(\text{flare}) + f(\text{quiescent})]$. It is 1.0 for $f(\text{quiescent}) = 0$, and 0.0 for $f(\text{quiescent}) = f(\text{flare})$. Lines have been grouped by $\log T_{\max}$, and clearly show increasing modulation with temperature, meaning that the flare was very hot. Features which give a better than 2.5σ confidence in the modulation have been emphasized.

The continuum modulation is defined similarly, except that T_{\max} is not well defined. Instead, we use a pseudo-temperature derived from the continuum band wavelength ($T = hc/k\lambda$), primarily to enable placement of continuum data on the same axis. The continuum is strongly modulated with about equal amplitude in each wavelength band. It is not very sensitive to temperature because its emissivity distribution is broad — a hot continuum adds significant flux at all wavelengths above a lower limit (or, at all lower pseudo-temperatures).

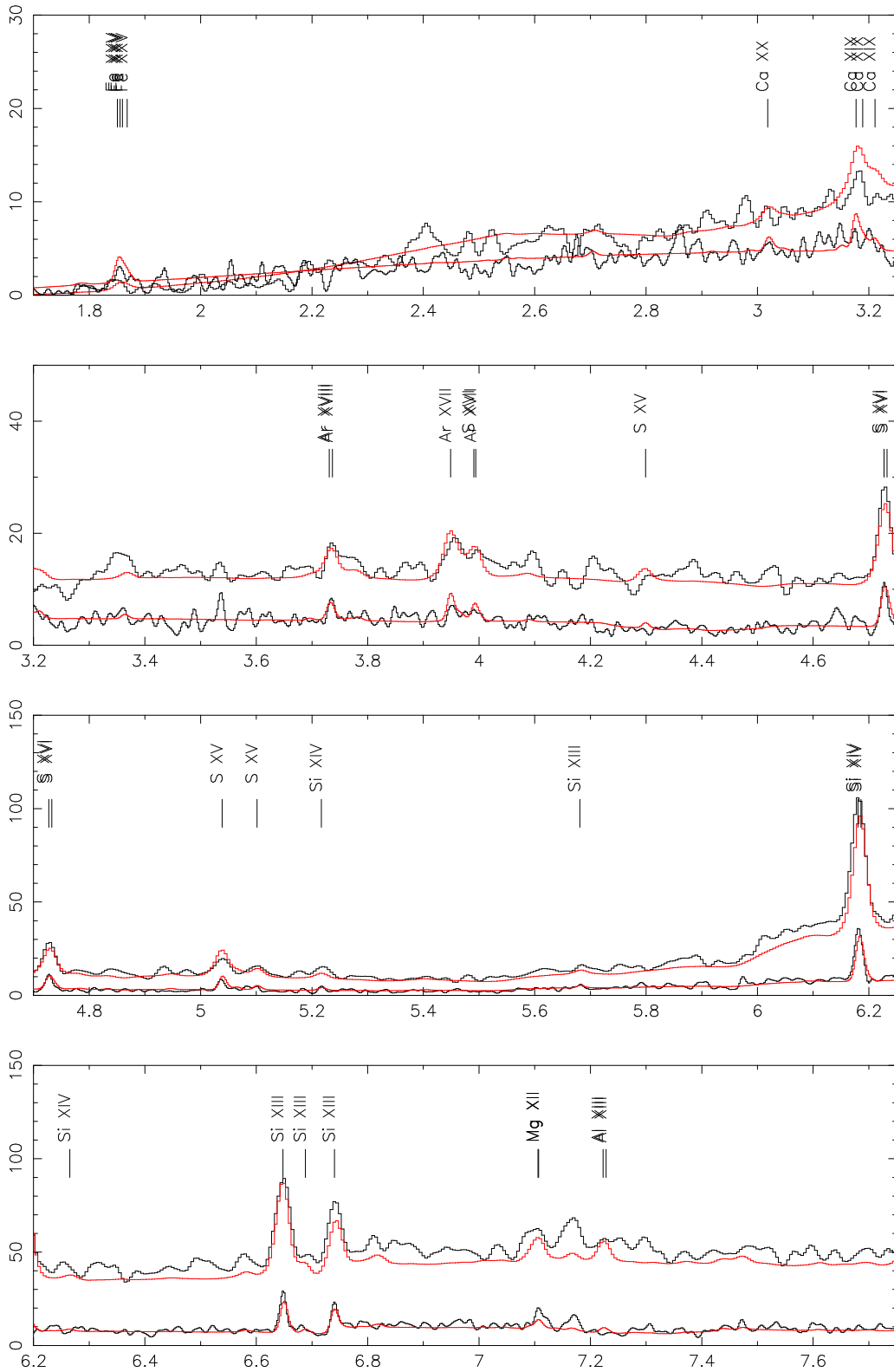


Fig. 5a.—

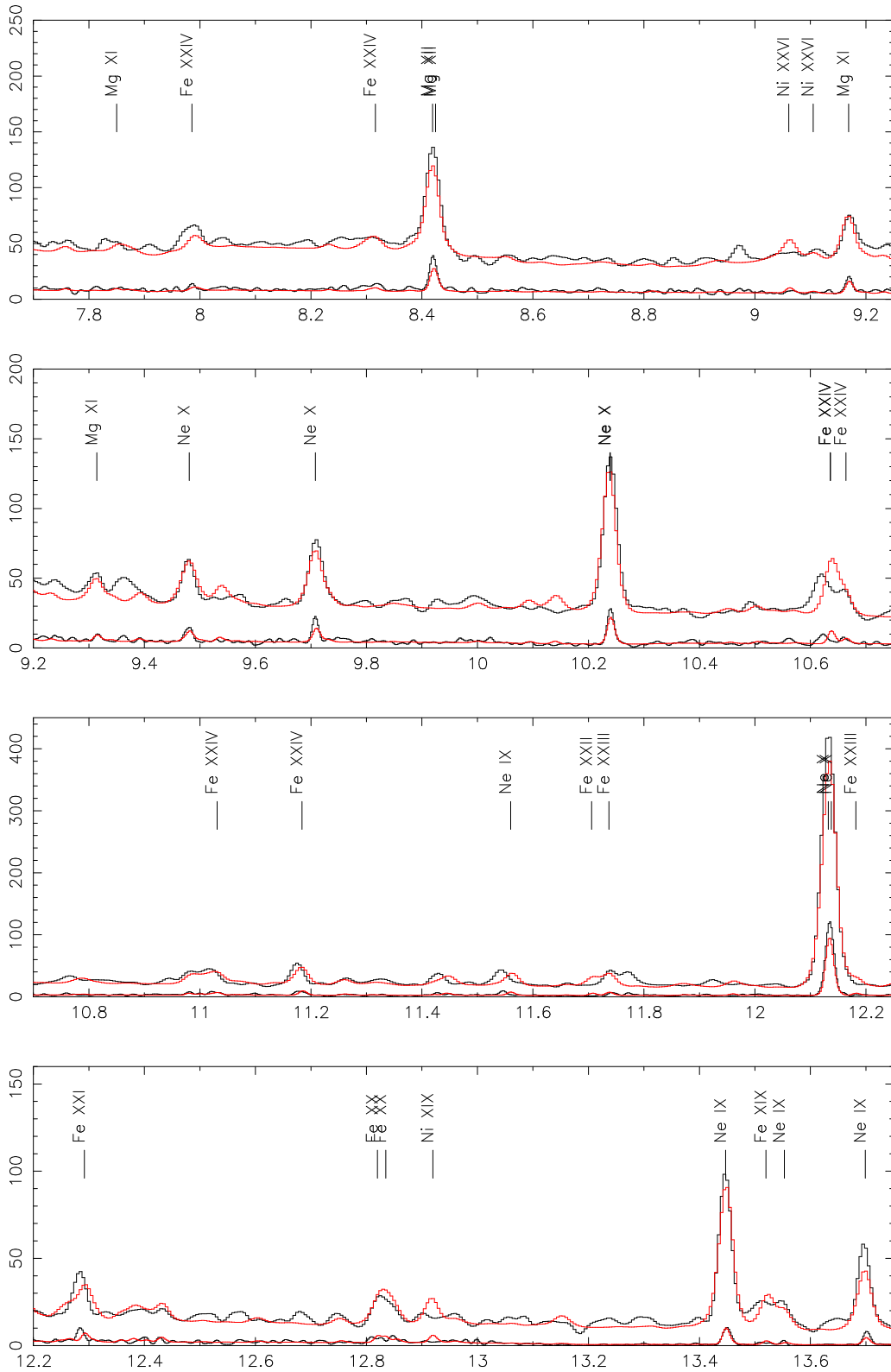


Fig. 5b.—

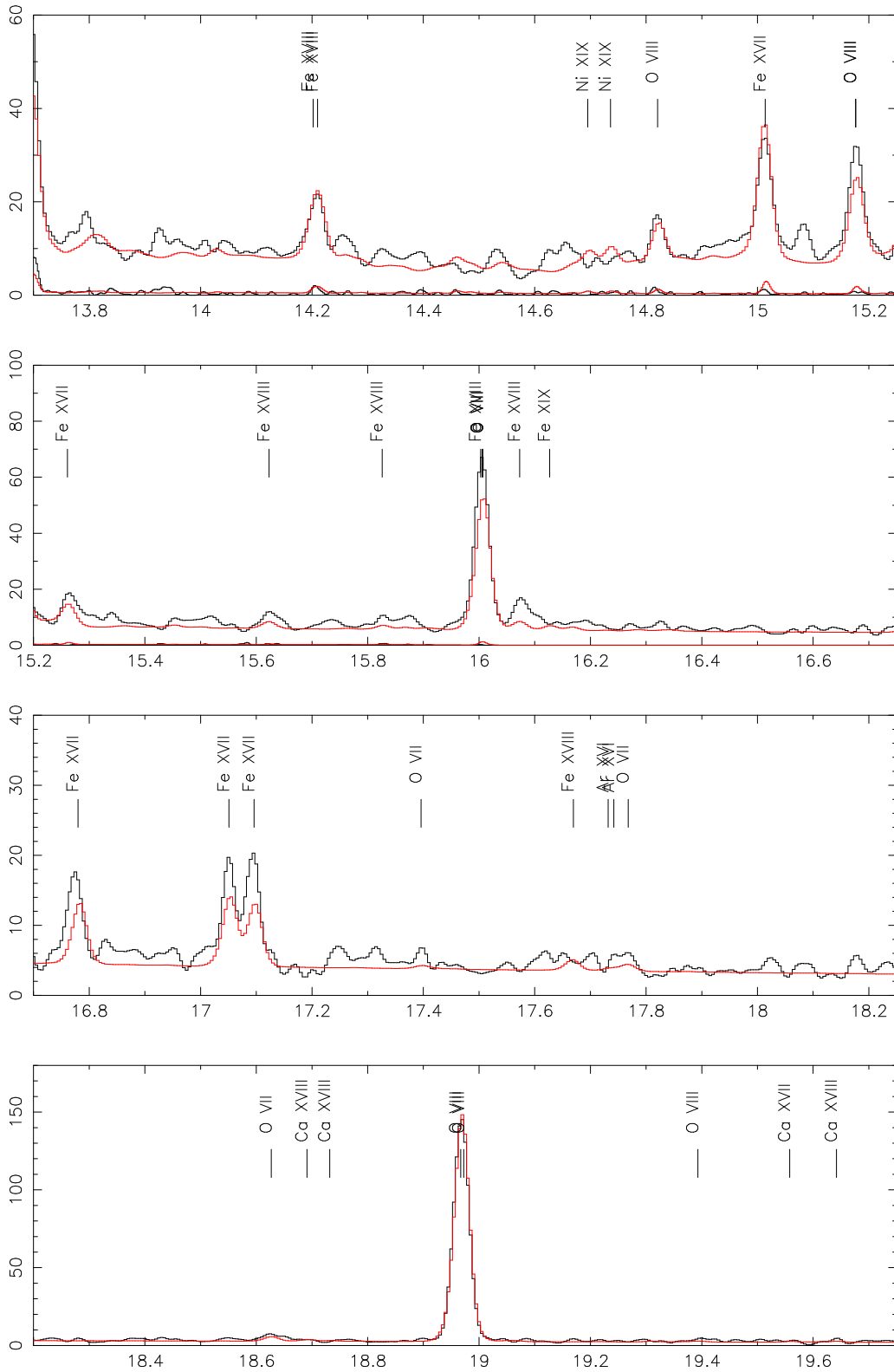


Fig. 5c.—

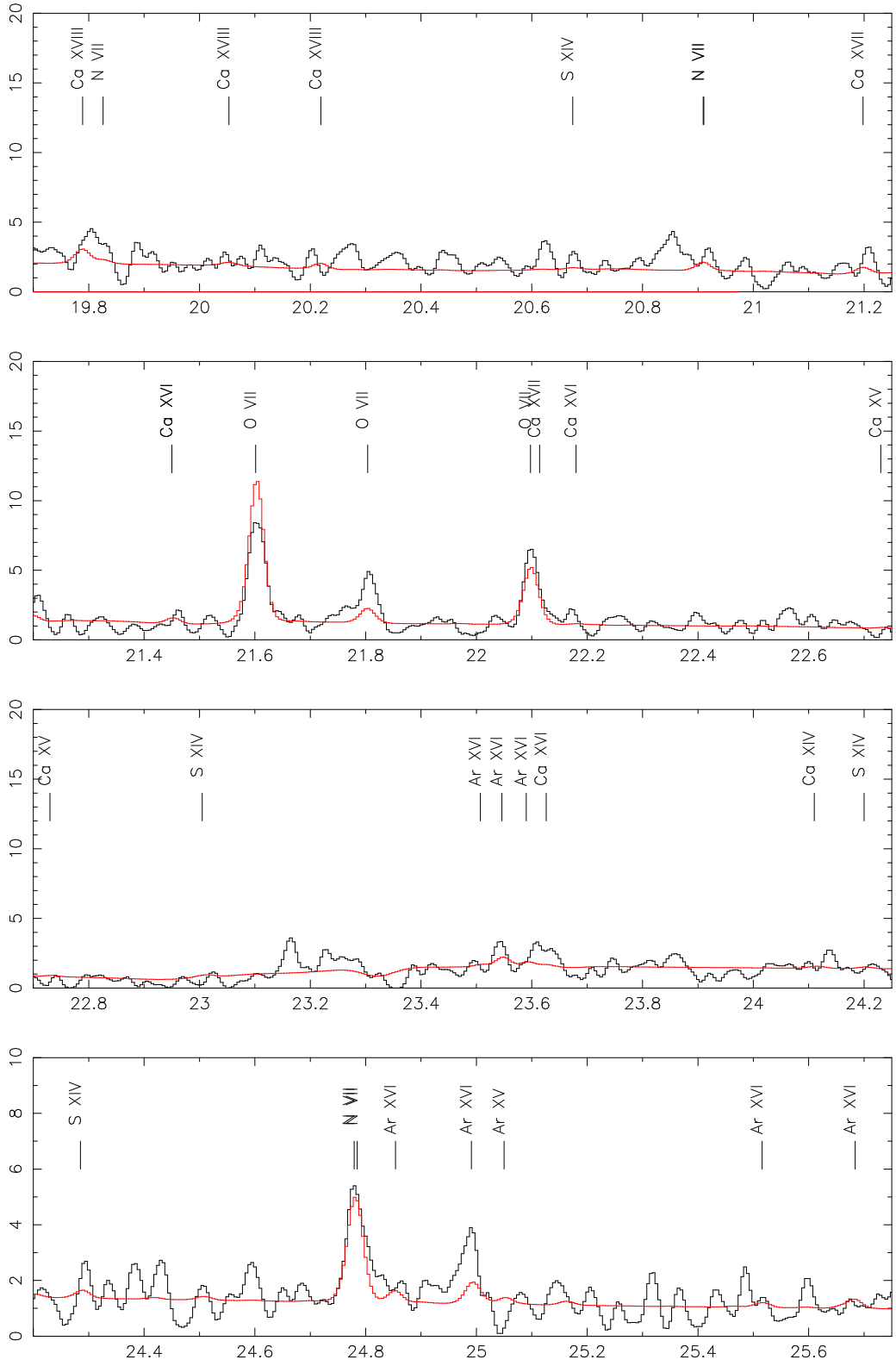


Fig. 5d.—

TABLE 1
EMISSION LINE MEASUREMENTS FOR ENTIRE SPECTRUM.

Line	λ_t^a	λ_o^b	σ	f_l^c	σ	f_c^d	σ	$\log T_{max}^e$
Fe XXV	1.8504	1.857	9.250e-03	13.27	12.84	384.3	156.8	7.8
Ar XVIII	3.7311	3.734	4.850e-03	14.31	5.49	1192.4	80.2	7.6
Ar XVII	3.9491	3.949	9.500e-03	6.75	6.01	1295.2	89.2	7.1
Ar XVII	3.9694	3.969	1.500e-02	13.30	26.01	1295.2	89.2	7.1
S XVI	4.7274	4.727	2.450e-03	49.33	8.92	1280.8	93.5	7.4
S XV	5.0387	5.037	1.450e-03	30.21	7.90	1293.4	76.1	7.2
S XV	5.1015	5.095	3.950e-03	17.35	7.75	1293.4	76.1	7.2
Si XIV	5.2180	5.221	4.950e-03	17.36	8.22	1381.5	102.8	7.2
Si XIV	6.1805	6.180	9.990e-05	80.10	5.33	1483.5	45.1	7.2
Si XIII	6.6479	6.648	1.200e-03	53.08	4.65	1476.9	40.6	7.0
Si XIII	6.6882	6.685	3.900e-03	8.40	3.74	1476.9	40.6	7.0
Si XIII	6.7403	6.740	9.990e-05	29.78	3.86	1476.9	40.6	7.0
Fe XXIV	7.9857	7.987	2.450e-03	12.30	3.23	1435.0	42.2	7.3
Mg XII	8.4193	8.420	5.007e-05	79.75	4.92	1412.6	44.8	7.0
Mg XI	9.1687	9.170	1.497e-04	40.63	4.85	1557.8	43.9	6.8
Mg XI ^f	9.2312	9.238	2.750e-03	10.17	4.04	1557.8	43.9	6.8
Mg XI ^f	9.3143	9.315	2.200e-03	13.95	4.31	1557.8	43.9	6.8
Ne X	9.4807	9.480	1.497e-04	38.20	5.38	1317.7	72.6	6.8
Ne X	9.7081	9.706	1.200e-03	62.06	5.20	1321.8	45.9	6.8
Ne X	10.239	10.240	5.007e-05	178.60	8.46	1188.1	95.2	6.8
Fe XXIV	10.636	10.620	5.007e-05	47.21	6.20	1391.8	55.1	7.3
Fe XXIV	10.664	10.660	2.999e-04	30.19	5.88	1391.8	55.1	7.3
Fe XXIV	11.184	11.176	1.400e-03	68.96	7.89	1214.9	88.1	7.3
Ne IX	11.560	11.545	1.001e-04	48.70	7.98	1408.1	77.6	6.6
Fe XXII-III	11.737	11.743	2.100e-03	50.74	7.93	1423.4	75.7	7.1
Ne X	12.132	12.132	2.999e-04	1110.30	21.60	1415.8	104.5	6.8
Fe XXI	12.292	12.285	2.999e-04	74.76	10.23	1537.0	103.3	7.1
Fe XX	12.820	12.821	2.450e-03	38.30	9.04	1375.1	110.0	7.0
Fe XX	12.835	12.843	2.450e-03	35.97	8.51	1375.1	110.0	7.0
Ne IX	13.447	13.446	1.250e-03	350.68	19.84	1283.8	107.5	6.6
Fe XIX	13.516	13.511	2.550e-03	72.40	6.49	1283.8	107.5	6.9
Ne IX	13.553	13.550	1.502e-04	75.58	12.10	1283.8	107.5	6.6
Ne IX	13.699	13.700	9.966e-05	203.29	17.78	1498.7	123.5	6.6
Fe XVIII	14.210	14.210	1.550e-03	69.39	15.21	1471.1	134.8	6.8
O VIII	14.821	14.825	4.950e-03	48.85	13.98	1377.9	111.3	6.5
Fe XVII	15.014	15.015	2.450e-03	113.65	17.53	1703.0	138.0	6.7
O VIII	15.176	15.180	1.001e-04	128.53	18.47	1339.7	159.7	6.5
Fe XVII	15.261	15.266	2.500e-03	54.62	13.85	1446.7	131.7	6.7
O VIII	16.006	16.010	2.350e-03	372.16	25.82	1548.3	119.2	6.5
Fe XVII	16.780	16.775	2.450e-03	97.53	19.92	1330.7	138.6	6.7
Fe XVII	17.051	17.050	2.450e-03	109.85	20.63	1075.7	153.0	6.7
Fe XVII	17.096	17.095	2.450e-03	126.49	21.40	1075.7	153.0	6.7
O VII	18.627	18.627	7.550e-03	45.27	24.42	1500.0	198.5	6.3
O VIII	18.967	18.972	1.950e-03	1958.10	73.90	1253.0	223.0	6.5
O VII	21.602	21.605	2.649e-03	222.86	52.68	1031.5	193.3	6.3
O VII	21.804	21.805	5.000e-03	130.96	48.33	1031.5	193.3	6.3

TABLE 1—*Continued*

Line	λ_t^a	λ_o^b	σ	f_l^c	σ	f_c^d	σ	$\log T_{max}^e$
O VII	22.098	22.095	2.600e-03	204.20	54.35	1031.5	193.3	6.3
N VII	24.779	24.784	5.051e-03	124.05	50.12	1116.2	311.6	6.3

^aTheoretical wavelengths of identification (from APED), in Å. If the line is a multiplet, we give the wavelength of the stronger component.

^bMeasured wavelength, in Å.

^cLine flux is 10^{-6} times the tabulated value in [phot cm⁻² s⁻¹].

^dContinuum flux is $10^{-6} \times$ the tabulated value in [phot cm⁻² s⁻¹ Å⁻¹].

^eLogarithm of temperature [Kelvins] of maximum emissivity.

^fBlended with high- n Ne x Lyman series lines.

TABLE 2
FLUX MODULATION LINE GROUPS

Ion Group	Wavelengths ^a	$f(Q)^b$	σ	$f(F)^b$	σ
Fe XXV	1.85	0	13	32	33
Fe XXIV	7.987, 10.620, 10.660, 11.176	98	15	231	25
Fe XXI-XXII	11.743, 12.285	109	19	146	26
Fe XVII	15.015, 15.266, 16.775, 17.050, 17.095	473	62	536	89
O VIII	14.825, 15.180, 16.010, 18.972	2345	119	2834	157

^aTheoretical wavelengths of identification (from APED), in Å. If the line is a multiplet, we give the wavelength of the stronger component.

^bSum of line fluxes, Q for Quiescent, and F for Flare; 10^{-6} times the tabulated value gives [phot cm⁻² s⁻¹].

TABLE 3
ABUNDANCE DETERMINATIONS

Element	FIP ^a	Quiescent ^b	Flare ^b	Total ^b
Mg	7.65	0.40	0.50	0.50
Fe	7.87	0.10	0.15	0.15
Si	8.15	0.45	0.50	0.45
S	10.36	0.80	0.45	0.65
O	13.62	1.10	1.05	1.10
N	14.53	0.6:	0.9:	0.6:
Ar	15.76	1:	1:	1:
Ne	21.56	2.20	2.60	2.35

^aFirst Ionization Potential, in eV

^bRatio of abundances to cosmic values of Anders and Grevesse (1989); uncertainties are about 20% (50% for values marked with “:”).